Optimization of synthesis parameters for O3-type NaNi0.33Fe0.17Mn0.5O2 Na-ion battery cathode materials

Electrochimica Acta 573 (2026) 149276

Contents lists available at ScienceDirect

Electrochimica Acta

journal homepage: www.journals.elsevier.com/electrochimica-acta

Optimization of synthesis parameters for O3-type $NaNi_{0.33}Fe_{0.17}Mn_{0.5}O_2$ Na-ion battery cathode materials

Valeria Sperati [a,b,c], Hamideh Darjazi [a,b], Alessandro Piovano [a,b], Marco Ricci [c], Claudio Gerbaldi [a,b,*], Giuseppe Antonio Elia [a,b,*], Remo Proietti Zaccaria [c]

[a] GAME Lab, Department of Applied Science and Technology (DISAT), Politecnico di Torino, Corso Duca degli Abruzzi, 24, Torino 10129, Italy
[b] National Reference Centre for Electrochemical Energy Storage Systems (GISEL) - INSTM, Via Giusti, 9, Firenze 50121, Italy
[c] Italian Institute of Technology, Via Morego 30, 16163, Genova, Italy

ARTICLE INFO

Keywords:
Sodium ion battery
Layered transition metal oxide
Cathode
Co-precipitation
P2/O3 phase coexistence

ABSTRACT

Layered transition-metal oxides are promising materials for sodium-ion battery cathodes, although their electrochemical performance is very sensitive to the synthesis conditions, which dictate phase composition and particle morphology. Here, we systematically investigate the influence of two key precursor co-precipitation parameters on the structural, morphological, and electrochemical properties of $NaNi_{0.33}Fe_{0.17}Mn_{0.5}O_2$ layered oxides: temperature (40 and 60 °C) and reaction time (9 and 24 h). Upon synthesis, temperature primarily influences particle agglomeration and crystallinity, while reaction time primarily regulates particle size and phase formation. Short synthesis times combined with higher temperatures favor the formation of an O3-dominant lattice with reduced aggregation, whereas longer times promote smaller particles and the development of mixed O3/P2 phases. Electrochemical characterization reveals that the sample obtained after co-precipitation at 60 °C for a shorter duration exhibits the best rate capability, reaching a specific capacity of 130 mAh g^{-1} at 0.1 C, and full capacity recovery at 0.4 C after C-rate test. Conversely, samples with a mixed O3/P2 phase exhibit better structural stability, retaining up to 70% of the initial capacity after 200 cycles. The novelty of this work lies in systematically decoupling co-precipitation parameters and directly correlating them with phase evolution and electrochemical performance. These results provide clear guidance for the controlled design of high-performance sodium-ion battery cathode materials.

1. Introduction

Layered transition-metal oxides are among the most promising positive electrode materials for sodium-ion batteries (NIBs), surpassing many polyanionic and framework-type chemistries due to their higher theoretical specific capacities, stemming from the absence of heavy polyanion groups. This advantage is further complemented by their pronounced structural versatility and wide compositional tunability [1, 2].This allows for varied compositions and stacking sequences, as well as high sodium-ion mobility in two-dimensional diffusion channels. This mobility is often accompanied by good electronic conductivity and a relatively simple, scalable synthesis.

Due to the success of lithium layered oxides (*e.g.*, 4 V-class NMC, $LiNi_xMn_yCo_zO_2$) in lithium-ion batteries, their sodium analogues have also been extensively investigated. Notably, the structural chemistry of sodium layered oxides is richer compared to their Li-based counterparts because Na^+ can occupy both octahedral (O) and prismatic (P) sites [3], whereas Li^+ resides exclusively in octahedral sites. This versatility allows a broader range of crystalline phases (e.g., O3, P2, P3), thereby enhancing the structural diversity and tunability of Na-layered oxides [4].

Among these, O3-type sodium layered oxides are particularly attractive for energy storage applications due to their stoichiometric sodium content (Na:TMs = 1:1, where "TMs" stands for transition metals). On the other hand, P-type phases typically show faster Na^+ diffusion kinetics and better structural stability, and they are only stabilized by sodium-deficient conditions (Na:TMs < 0.8:1) [5,6], which reduces the achievable capacity unless compensated by sacrificial additives or complex cell design strategies [7–9]. Therefore, O3-type structures remain the most practical choice for large-scale development.

* Corresponding authors at: GAME Lab, Department of Applied Science and Technology (DISAT), Politecnico di Torino, Corso Duca degli Abruzzi, 24, Torino 10129, Italy.
E-mail addresses: claudio.gerbaldi@polito.it (C. Gerbaldi), giuseppe.elia@polito.it (G.A. Elia).

https://doi.org/10.1016/j.electacta.2026.149276
Received 9 April 2026; Received in revised form 12 May 2026; Accepted 2 June 2026
Available online 3 June 2026

Extensive research has shown that incorporating manganese (Mn), iron (Fe), and nickel (Ni) into the TM layer of O3-type oxides can improve their electrochemical performance [10–12] while keeping costs down. Since each TM independently influences the redox activity, structure, and stability of the end product, achieving the optimal TM balance is essential for developing a material that exhibits both structural stability and high practical capacity. In this study, the reactant ratio was selected to match the desired TM stoichiometry in the final product and to promote the formation of a specific phase structure, as detailed in Section 2.1. Manganese, although abundant and inexpensive, has an inherent limitation due to the Jahn–Teller effect, which arises from the presence of Mn^{3+} in octahedral coordination. In an octahedral environment, the 3d orbitals of manganese are split into two energy levels (t_{2g} and e_g). For Mn^{3+}, the uneven distribution of electrons in these orbitals causes distortion of the MnO_6 octahedra, generating local lattice strain and breaking the symmetry of the TMO_2 slabs. During repeated cycling, the accumulation of these distortions promotes slab gliding, facilitates TM migration, and favors irreversible phase transitions that lead to structural degradation [13,14]. However, when present in its Mn^{4+} oxidation state, manganese provides structural stability; without Jahn-Teller distortion. In this work, its content was maintained at around 50% to prevent phase transitions and structural collapse caused by the de-/sodiation process. Partial substitution of Mn with Fe mitigates distortions, increases interlayer spacing, and enhances structural stability at high states of charge; in addition, it provides access to the $Fe^{4+/3+}$ redox couple, which is typically inactive in lithium systems. However, an excessive amount of iron within the structure can lead to a massive migration of Fe^{3+} into the Na layer, where it acts as a structural pinning center. This hinders reversible slab gliding and lead to partial irreversibility of the phase transition and, consequently, reduced capacity retention. Therefore, for this work, its proportion was restricted to below 20%. Nickel increases the available capacity via its $Ni^{4+/2+}$ redox activity, although its incorporation into the compound is more sensitive to synthesis conditions [15–17]. Here, nickel was kept below 40% to maximize its redox contribution while minimizing the formation of NiO-type impurities.

Despite the extensive exploration of layered oxides as positive electrodes for NIBs, the variability in reported performances is often linked to differences in synthesis protocols, especially for multi-cation systems [18–26]. Among the available synthetic routes, co-precipitation stands out for producing homogeneous particle morphology and precise compositional control, both of which are crucial for achieving phase purity and optimal electrochemical performance. Compared to solid-state or sol-gel synthesis, co-precipitation enables better homogeneity of multiple transition metals; however, it involves a more complex and delicate procedure. The process, described by the dissolution-recrystallization mechanism [27,28], generally involves two stages: (i) co-precipitation of TM hydroxides (precursors) from their sulfate/nitrate in aqueous ammonia, and (ii) calcination with sodium carbonate to form the layered oxide. During co-precipitation, parameters such as ammonia concentration, pH, metal ion complexation, and precipitation kinetics govern the morphology, composition, and homogeneity of the precursor. These, in turn, directly affect phase purity, crystallinity, and the electrochemical behavior of the final material.

Before discussing the present results, it is essential to summarize the existing literature on key synthesis parameters in co-precipitation (see also Table S1 in the Supporting Information). Previous studies have shown that temperature and reaction time are critical, interdependent parameters in co-precipitation processes, governing the physicochemical and morphological properties of the resulting precursors. Temperature plays a complex role in this process: it influences the solubility of transition metal salts, the stability of intermediate metal-amine complexes, and the kinetics of crystal nucleation and growth. Generally, elevated temperatures accelerate the dissolution-recrystallization mechanism, yielding higher crystallinity, reduced primary particle aggregation, and imparting a more uniform particle morphology [29]. However, slight deviations in temperature can shift equilibrium states, potentially inducing phase impurities or uncontrolled precipitation, especially in systems with mixed transition metals, such as nickel, iron, and manganese, as in this case. Reaction time is equally critical and strongly linked to the reagent addition rate (flow rate) [30]. This parameter influences supersaturation dynamics, directly affecting particle size distribution and agglomeration. Decreasing the flow rate prolongs the reaction, allowing sufficient time for particle crystallization, avoiding the formation of amorphous by-products. However, if the rate is too low, the growth of primary particles becomes more favorable than their nucleation, increasing average particle size.

While the basic principles of nucleation and growth are well established, the specific roles of reaction duration and temperature in controlling particle size, morphology, and phase evolution remain insufficiently explored, especially for positive electrodes in NIBs. Extended reaction times and elevated temperatures can alter the particle size distribution, crystal growth dynamics, and the degree of cation mixing, thereby affecting electrochemical performance. Furthermore, the dynamic equilibrium between metal-ammonia complexes and metal hydroxides [31] can shift with both reaction time and temperature, affecting the quality and reproducibility of the precursor.

In this work, we investigate how time and temperature affect the formation of the hydroxide precursor and, consequently, the properties of the final O3-type $NaNi_{0.33}Fe_{0.17}Mn_{0.5}O_2$ layered oxide. While these variables act exclusively during the precursor synthesis step, their impact propagates to the final material, influencing its phase composition, morphology, and electrochemical behavior after calcination.

All other synthesis variables were held constant to isolate the impact of these two parameters during the co-precipitation. By correlating precursor formation conditions with final material properties and electrochemical performance, this study aims to clarify the synthesis–structure–function relationship and provide guidelines for optimizing co-precipitation routes for layered sodium cathode materials.

2. Experimental

2.1. Material synthesis

$NaNi_{0.33}Fe_{0.17}Mn_{0.5}O_2$ was synthesized via solid-state reaction between $TM(OH)_2$ (i.e., $Ni_{0.33}Fe_{0.17}Mn_{0.5}(OH)_2$) and Na_2CO_3 (Fig. 1a). The hydroxide precursor was prepared in advance by coprecipitation, as schematically illustrated in Fig. 1b.

The transition-metal sulfate salts, namely $NiSO_4{\bullet}6H_2O$ (Sigma Aldrich, 98%), $FeSO_4{\cdot}7H_2O$ (Sigma Aldrich, 97%), and $MnSO_4{\cdot}H_2O$ (Sigma Aldrich, ReagentPlus® ≥ 99%), were dissolved separately in Milli-Q water in stoichiometric proportions and then mixed to obtain a 2 mol L^{-1} total metal solution. This solution was collected in a round-bottom three-neck flask and degassed by stirring under a continuous flow of N_2 at the target temperature. In parallel, NaOH and NH_4OH solutions were prepared with $[NaOH]:[TM]_{tot}$ = 2:1 and $[NH_4OH]:[TM]_{tot}$ = 1.1:1. and loaded into two synchronized syringe pumps and simultaneously introduced into the reaction flask at identical flow rates to initiate coprecipitation. In a typical reaction setup, each syringe was loaded with 13.75 mL of solution, and the flow rate was set according to the desired reaction time (either 13.75 mL/9 h or 13.75 mL/24 h). The total reaction volume, considering the precursor solution, NaOH solution, and NH_4OH solution, was 100 mL, and the pH in the 3-neck flask is pH = 11, in agreement with the literature.

Thus, four samples were synthesized using different combinations of two temperatures (i.e., 40 and 60 °C) and two reaction times (i.e., 9 and 24 h, obtained by adjusting the flow rate accordingly) during co-precipitation, to obtain the samples denoted as follows (and shown in Fig. S1): S1 (9 h, 60 °C), S2 (9 h, 40 °C), S3 (24 h, 60 °C) and S4 (24 h, 40 °C).

The precipitation reaction was conducted at a fixed stirring speed (800 rpm). Afterward, the precipitate was filtered, washed several times

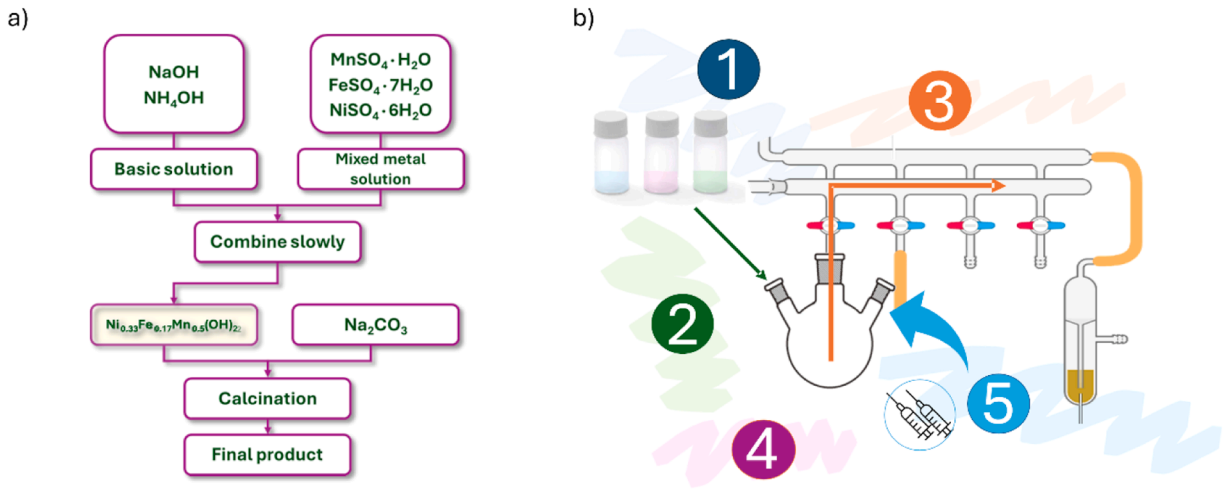

Fig. 1. a) Schematic summary of the synthesis procedure, outlining the progression from the initial mixing of reagents through the subsequent reaction stages leading to the final product. b) Schematic representation of the preparatory steps to be addressed before the co-precipitation phase: (1) preparation of Fe:Mn:Ni solutions; (2) transfer of separately dissolved salts to the reaction flask; (3) degassing under N2 flow (4) loading NaOH and NH4OH in two syringes; and (5) initiation of co-precipitation using synchronized syringe pumps.

to remove the residual sodium and sulfur species, and then dried under vacuum at 80 °C overnight. The so-obtained precursor was thoroughly mixed with Na_2CO_3 (in 10% stoichiometric excess, Na:TMs = 1.1:1) in an agate mortar. The mixture was calcined for 10 h at 900 °C (heating rate of 5 °C min^{-1}) in air to obtain $NaNi_{0.33}Fe_{0.17}Mn_{0.5}O_2$ powder. All other synthesis variables (e.g., pH, stirring rate, metal ratio, ammonia concentration, and calcination conditions) were kept constant to focus specifically on the influence of co-precipitation time and temperature on the final properties of the oxide materials.

2.2. Material characterization and electrochemical tests

The relative concentration of metals in the samples was determined by inductively coupled plasma optical emission spectrometry (ICP-OES). The crystalline structure was identified by X-ray diffraction (XRD, Panalytical, Xpert3 MRD) using the Cu Kα radiation in the 2θ range of 10°-70°. Scanning electron microscopy (SEM, JCM-6000Plus, JEOL) was used to examine the morphology of the samples. The XRD measurements at different temperatures were carried out using an Empyrean Series III diffractometer (Malvern Panalytical) equipped with an HTK1200N heating chamber (Anton Paar). The first diffraction pattern was recorded at RT after mixing the hydroxide precursor with sodium carbonate. The sample was then heated at a rate of 3 °C min^{-1} to 700 °C, where a second pattern was collected. Then, diffraction patterns were collected every 50 °C up to 900 °C at the same heating rate. Finally, the sample was cooled back to RT at 3 °C min^{-1}.

The electrodes were prepared by mixing the active material with carbon black (Super C65, Sigma Aldrich) as electronically conducting additive and polyvinylidene fluoride (PVDF, Sigma Aldrich) as binder in 8:1:1 weight ratio. The slurries were obtained by adding an appropriate amount of N-methyl-2-pyrrolidone (NMP, Sigma Aldrich), followed by homogenization using a THINKY ARE-250 mixer. The resulting slurry was cast onto aluminum foil and vacuum-dried at 120 °C. The electrodes were then punched into 10 mm diameter disks, having an average active material loading of 3 mg cm^{-2}. They were assembled into three-electrode Swagelok-type sodium-metal cells, employing a glass fiber separator (Whatman GF/A) imbibed with 1 M $NaPF_6$ in EC:DMC (1:1 v:v). Sodium metal was used as both counter and reference electrodes. All of the abovementioned procedures were performed under the controlled atmosphere of an Ar-filled glovebox (MBRAUN UNIlab, O_2 and H_2O content below 0.5 ppm). Galvanostatic cycling was performed at various C-rates within the voltage window 2-4 V *vs.* Na^+/Na at room temperature (≅ 25 °C) using a BT-2000 battery testing system (Arbin, USA). 1 C is assumed as 140 mA g^{-1} [12,32].

Differential capacity analysis (DCA) was performed by calculating the derivative of the transferred charge as a function of working electrode potential using OriginPro version 2022 (OriginLab Corporation, Northampton, MA, USA), following the procedure reported by Diolaiti *et al.* [33]. As a preliminary step to denoise, a uniform, linearly spaced curve interpolating the data and containing 100 points is calculated using the 'Interpolate/Extrapolate' function. After denoising, the derivative of this curve is calculated with the 'Differentiate' function.

3. Results and discussion

As described in the introduction, the TMs ratio was carefully selected to promote the formation of the O3-type layered oxide structure (Fig. S2). This was done by calculating the cationic potential (Φ_{cation}) [34,35], which can be used to predict the stacking type structure through Equation 1:

$$\Phi_{cation} = \frac{\overline{\Phi_{TM}} \cdot \overline{\Phi_{Na}}}{\overline{\Phi_O}} \quad (1)$$

where $\overline{\Phi_{TM}}$ is the weighted average ionic potential of TMs, defined as $\overline{\Phi_{TM}} = \sum \frac{w_i n_i}{R_i}$; here, w_i is the molar fraction of the i^{th} TM among TMs (*e.g.*, 1/3 for TMs in NMC111), n_i its charge, and R_i its radius. $\overline{\Phi_{Na}}$ is the weighted average ionic potential of Na, defined as $\overline{\Phi_{Na}} = \frac{x_{Na}}{R_{Na}}$, where x_{Na} is the stoichiometric coefficient of Na, and $\overline{\Phi_O}$ corresponds to the ionic potential of oxygen. Then, by plotting $\overline{\Phi_{Na}}$ against Φ_{cation} it is possible to establish a composition-structure phase boundary between the P2 and O3 phases. Even though the cationic potential is a useful predictor for guiding the compositional design of layered oxides toward the preferred stacking sequence, it does not guarantee the formation of the intended phase. Especially in multicomponent systems, synthesis-related factors strongly influence the actual resulting structure. Therefore, obtaining phase-pure, cycling-resilient materials requires both compositional tuning and precise control over synthesis conditions. In this study, we demonstrate that controlling these parameters, nominal temperature and duration of the co-precipitation step, yields a hydroxide precursor and a resulting layered oxide with composition, structure, and morphology close to the target.

The ICP-OES analysis (Fig. 2a) shows that the stoichiometry of the samples is consistent, independent of the conditions in which the

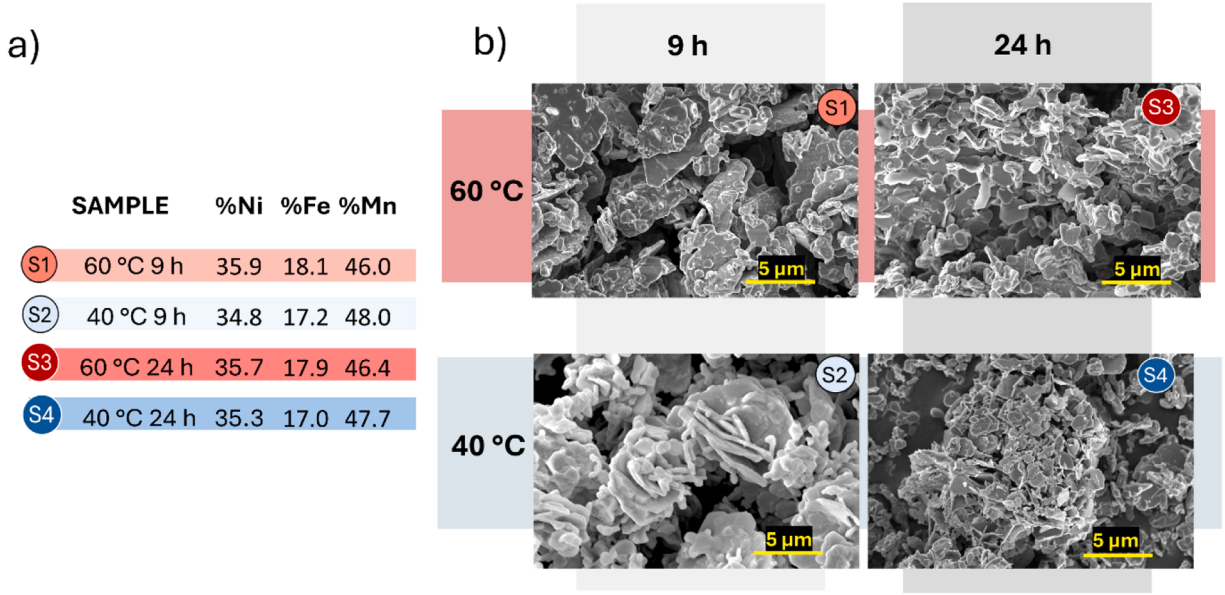

Fig. 2. a) Stoichiometric ratio of TMs (Ni, Fe, and Mn) in the active material obtained by ICP-OES expressed as a percentage of the total TM content. Color code: S1 – light red, S2 – light blue, S3 – red, and S4 – blue. b) SEM micrographs of the synthesized samples, all recorded at the same magnification with a scale bar of 5 µm.

precursor is synthesized. The average atomic fractions of TMs are Ni = 35.4 at%, Fe = 17.6 at%, and Mn = 47.0 at%. The morphological analysis by scanning electron microscopy (SEM) reveals, for all four samples, agglomerates of particles with sizes ranging between 1 and 10 µm (Fig. 2b). Notably, samples obtained at 60 °C are less aggregated than those synthesized at 40 °C, while samples obtained with longer synthesis times (*i.e.*, with a lower flow rate) show a clear reduction in primary particle size. This is also confirmed by the SEM micrographs obtained on the precursors (Fig. S3a). In addition, XRD patterns collected on the $TM(OH)_2$ precursor materials (Fig. S3b) indicate that samples S1 and S3 exhibit more defined and sharper diffraction peaks, suggesting a higher degree of crystallinity. These observations confirm that temperature mainly governs the degree of aggregation, whereas synthesis duration predominantly influences the size of the primary particles. From a thermodynamic perspective, the reduced aggregation at higher temperatures can be rationalized in terms of entropy contributions: as temperature increases, the entropy and thermal motion of the system rise, inhibiting particle agglomeration [36]. Instead, the observed decrease in particle size with longer synthesis times can be attributed to nucleation kinetics. This behavior can be explained by the interplay between the reagent addition rate and mixing. When flow rates are low, reagents are added slowly, creating a uniform supersaturation throughout the solution. This promotes the formation of numerous nucleation sites, resulting in smaller primary particles. On the other hand, higher flow rates lead to quick reagent addition, creating localized supersaturation gradients that favor the growth of existing nuclei rather than new ones. Moreover, as proposed by Bianchini et al. [37], the lattice evolves through the initial formation of the metastable O3 structure, which then progressively transforms into the more stable P2 phase via a reconstructive nucleation-and-growth mechanism, in which multiple P2 nuclei form within each parent grain, leading to smaller crystallites as a natural outcome of the transformation [26]. Notably, a reduction in primary particle size is already observed in the $TM(OH)_2$ precursor materials prior to calcination, confirming that particle size reduction also originates independently from nucleation kinetics during the co-precipitation step. Therefore, the smaller particle size observed with longer synthesis times reflects the combined influence of these two concurrent effects, consistent with the higher P2 fraction confirmed by XRD.

Together, these effects determine the growth and coalescence of primary particles, explaining the combined influence of temperature and synthesis duration on morphology. Additional SEM images at lower magnification are provided in Fig. S4.

Fig. 3 shows the XRD patterns of all samples, grouped according to synthesis duration. All four diffraction patterns match an O3-type layered oxide phase (*R-3m*, 166) with the characteristic ABCABC stacking sequence [38]. However, several minor reflections attributable to secondary phases are also observed, likely due to the multiple steps involved in the synthesis route; the XRD patterns were indexed against ICSD 221352 and ICSD 147522 for the O3-type and P2-type phases, respectively. Notably, a weak reflection at ~43.3° indicates the presence of NiO (*Fm-3m*, 225), labeled with a hash ("#"), a commonly reported secondary phase in this class of materials [39–42]. Although NiO was employed as a precursor during calcination [43], its presence in the final product is likely due to air exposure during the measurement, highlighting the air sensitivity of these layered oxides. Notably, these secondary phases are much more prominent in the post-annealing XRD patterns collected after cooling than in those obtained directly at the end of calcination (see Fig. S5), supporting the conclusion that they form upon contact with air. This highlights the importance of handling these materials in an inert environment, such as a glovebox, to prevent the formation of surface contaminants [44,45].

Additional reflections corresponding to the P2 phase (*$P6_3/mmc$*, 194, ABBA stacking sequence), labeled with a green asterisk ("*"), are present in the diffractograms of all samples [46] with markedly higher intensity for S3 and S4 (longer reaction times), in accordance with the reduction in particle size as observed in the SEM micrographs (Fig. 2b). For a fixed synthesis time, the reflections of the P2 phase are more intense for the samples synthesized at lower temperatures. This is more evident in the enlarged views of the (003) and (104) peaks. For example, the peak at ~16.2°, indexed to the (003) reflection of the O3 phase, displays a shoulder at ~15.9°, indexed to the (002) reflection (green) of the P2 phase, which is also its most intense reflection. Further confirmation of the presence of the P2 phase comes from the peaks in the ranges of ~31°-37.1°, indexed to its (004) and (102) reflections. The gradual decrease in peak intensity with reduced synthesis time and increased synthesis temperature suggests partial suppression of P2 phase formation under those conditions.

Finally, a peak at ~30.1° appearing only for samples S3 and S4 can be indexed to $MnCO_3$ (*R-3c*, 167), labeled with "●". This phase is likely a

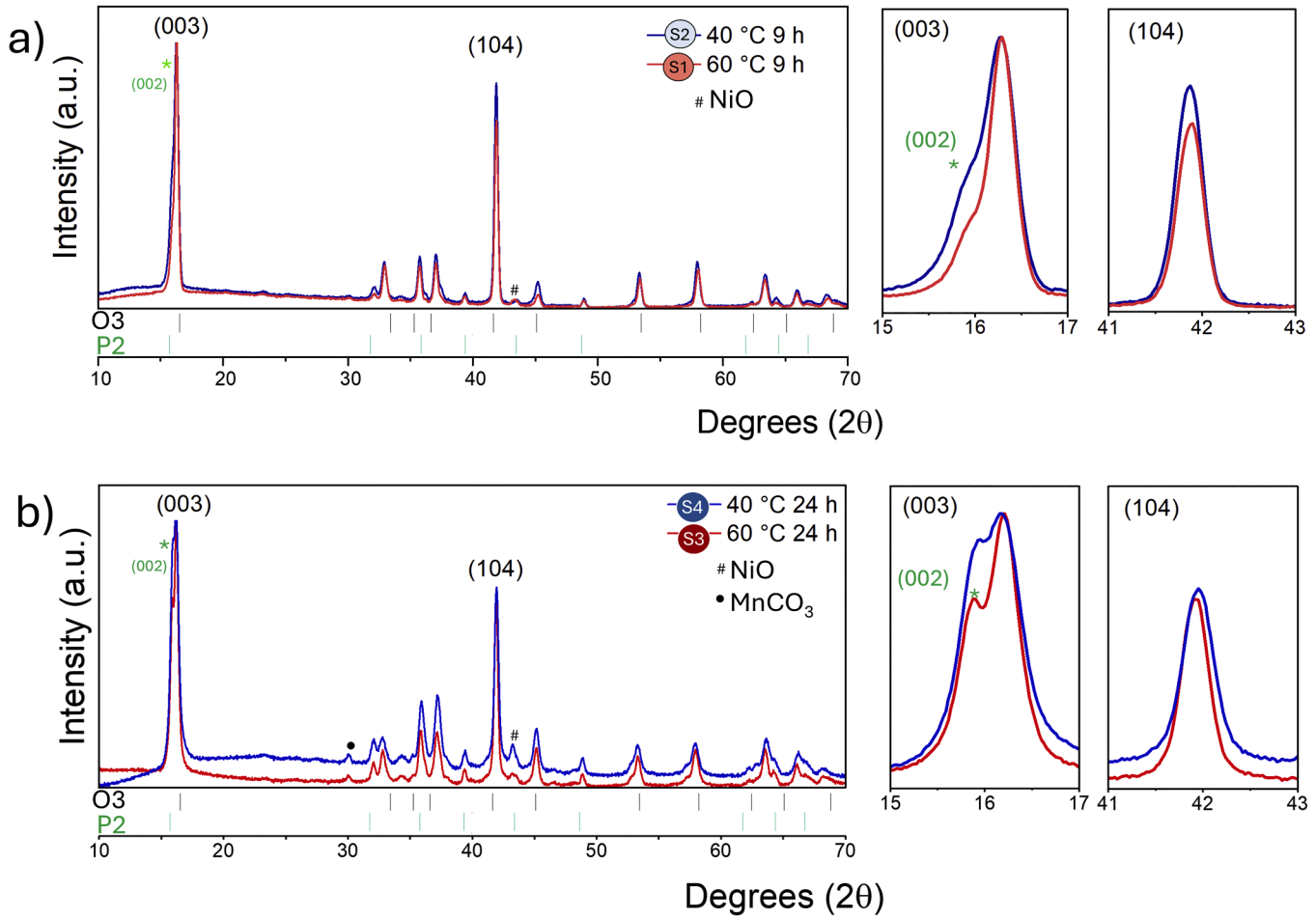

Fig. 3. a) Diffraction patterns of samples S1 and S2 (9 h synthesis). b) Diffraction patterns of samples S3 and S4 (24 h synthesis). Enlarged views of the (003) and (104) reflections are included for better clarity. In both panels, all detected impurity phases are reported and indicated in the legend.

byproduct of unreacted Mn species during co-precipitation, which converted to $MnCO_3$ upon air exposure before calcination. The incomplete incorporation of Mn may be attributed to the instability of Mn $(OH)_2$ in alkaline solutions [47], where Mn^{2+} is prone to oxidation into Mn^{3+} (*e.g.*, MnOOH) due to the greater thermodynamic stability of Mn^{3+} compared with Mn^{2+}. Even under N_2 atmosphere, prolonged synthesis times increase the possibility of forming Mn^{3+}-based impurities.

Fig. 4a shows the rate capability of the cathodes, evaluated by galvanostatic cycling at increasing C-rates as indicated in the figure, within the voltage window 2 - 4 *vs.* Na^+/Na. After C-rate testing, the sample was further cycled at 0.4 C to assess capacity retention. The results indicate significant differences among the samples, with S1 delivering the highest capacity at all C-rates (130, 118, 107, 86, 70, 45, and 103 mAh g^{-1}), while S4 shows significantly lower capacities (57, 52, 44, 32, 22, 10, and 43 mAh g^{-1}), indicating a lower rate capability. The rate capability trend is S1 > S3 > S2 > S4. The superior performance of S1 can be attributed to its crystal structure, which facilitates the diffusion of Na^+. Even though all samples show a progressive capacity decrease with increasing C-rate, they were able to sustain cycling up to high 4 C without permanent function loss (S1 still delivering a capacity of 45 mAh g^{-1}), as highlighted by complete capacity recovery upon returning to 0.4 C (103 mAh g^{-1} for S1, 60 mAh g^{-1} for S3, 50 mAh g^{-1} for S2, and 43 mAh g^{-1} for S4), confirming good structural stability. Samples S3 and S4 show slightly lower coulombic efficiency (CE) than S1 and S2, consistent with their smaller particle size. Indeed, the larger surface area of smaller particles enhances electrolyte contact but also promotes a more extensive formation of electrode/electrolyte interphase, decreasing CE. The complexity of these multiphase systems, where O3- and P2-type stacking sequences coexist and evolve during cycling, makes quantitative kinetic analysis via EIS, GITT, or CV a non-trivial task, which will thus be the object for future mechanistic studies [48].

The long-term cycling performance at 0.4 C (Fig. 4b) further illustrates the electrochemical stability. During prolonged cycling, CE stabilizes at ~98% for all samples, indicating the formation of a stable electrode/electrolyte interphase and highly reversible sodiation/desodiation. After 200 cycles, capacity retention is approximately 60% for S1, 65% for S2, and 70% for both S3 and S4. The lower capacity retention of S1 and S2 may be attributed to their higher fraction of the O3 phase, which is more prone to irreversible O3 → P3 transitions, transition-metal migration, and accumulated lattice strain during prolonged cycling. These processes can result in local structural collapse, stacking faults, and eventual formation of electrochemically inactive phases (*e.g.*, rock-salt-like domains), especially near the particle surface, thus compromising the electrochemical performance due to the loss of active Na sites [49].

Fig. 5 shows the differential capacity profiles of the samples, obtained from the voltage-capacity data (shown in Fig. S6 as voltage *vs.* capacity profiles) and displayed for selected cycles (2nd, 5th, 10th, and 15th). As expected, samples S1 and S2 exhibit similar features; so do S3 and S4, defining two distinct groups. Samples S1 and S2 exhibit pronounced peaks in the 2.8 - 3.1 V region, associated with the Ni^{3+}/Ni^{2+} couple and the O3-P3 transition, indicating a high initial fraction of the O3 phase. The progressive broadening and slight shift of these peaks with cycling suggest gradual structural rearrangements and the onset of transition irreversibility under repeated sodiation/desodiation. In addition to the Ni-related features, the broad features between 3.3 and

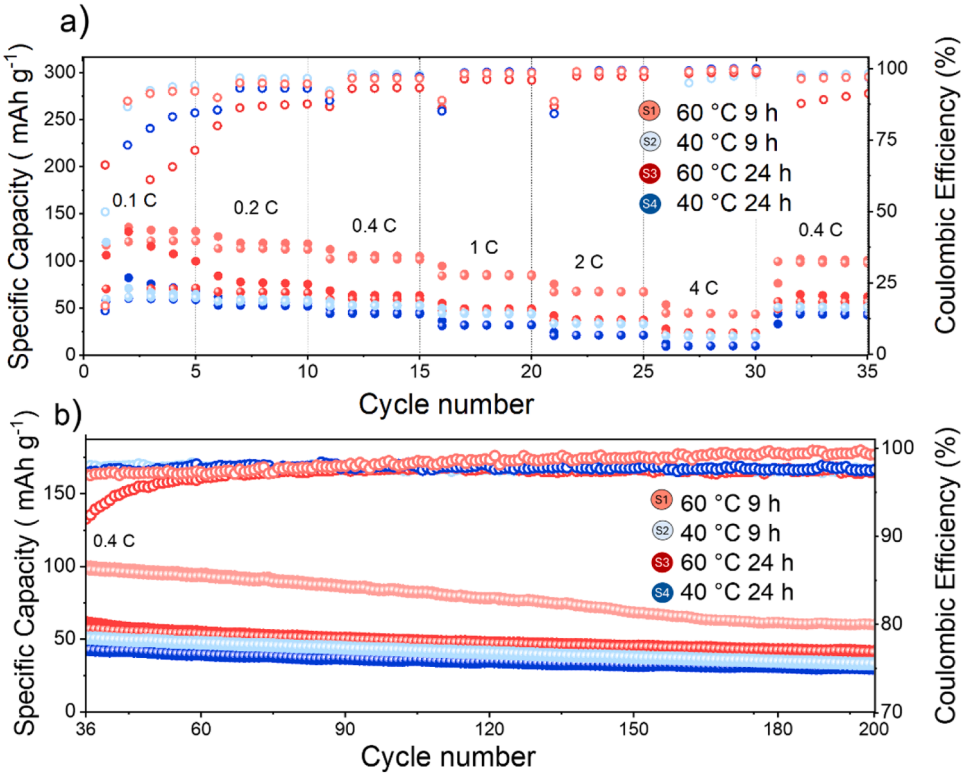

Fig. 4. a) Specific capacity of S1-S4 measured at different C-rates (0.1 C, 0.2 C, 0.4 C, 1 C, 2 C, 4 C, and back to 0.4 C). b) Specific capacity of S1-S4 measured at a constant C-rate (0.4 C) for 200 cycles. The color code used in both graphs is as follows: S1 – light red, S2 – light blue, S3 – red, and S4 – blue.

3.7 V reflect overlapping contributions from the Fe^{4+}/Fe^{3+} and Ni^{4+}/Ni^{3+} redox activity and the characteristic changes associated with Na^{+}/vacancy ordering couple and the subsequent P3-P3'' phase transition [50,51]. The complexity and broadening in this region are consistent with multiple, partially overlapping processes and structural modulations during cycling. In contrast, S3 and S4 display broader, less intense peaks across the voltage range, with much less pronounced features, especially in the lower-voltage region. This indicates a lower initial contribution of the O3 phase and a greater relative contribution of P-type stacking or mixed stacking sequences. The redox peaks in these samples also evolve more slowly with cycle number, implying more stable local environments and reduced structural rearrangements, which aligns with the more gradual capacity fade and better retention observed during cycling.

Overall, S1 demonstrated the best electrochemical performance in terms of rate capability and specific capacity, likely due to the dominant O3 phase. However, this also results in faster capacity fading upon cycling, which can be attributed to irreversible phase transitions typical of O3-type structures. Sample S3, synthesized at the same temperature (60 °C), showed slightly lower performance but greater structural stability. This is probably due to decreased particle aggregation at this temperature, as shown in the SEM micrographs. Sample S2, obtained at 40 °C for 9 hours, shows intermediate behavior, combining relatively high capacity with moderate retention, consistent with its predominantly O3-type phase. Ultimately, Sample S4 exhibits the worst electrochemical performance, in agreement with the structural and morphological characterization.

4. Conclusion

This study focused on a systematic investigation of how synthesis conditions, particularly temperature and time, influence both the structural and electrochemical properties of $NaNi_{0.33}Fe_{0.17}Mn_{0.5}O_2$. The choice of synthesis conditions is based on the chemistry of the co-precipitation process. Temperatures above 60 °C were intentionally avoided because higher temperatures promote the formation of secondary Mn-based oxyhydroxides and mixed oxide species. This occurs because Mn is more prone to oxidation in alkaline solution at higher temperatures, leading to deviations from the desired stoichiometry. Regarding synthesis time, significantly shorter durations do not allow the precipitation process to be completed. Under these conditions, part of the metal ions remain in solution or form soluble complexes; the initially formed nuclei remain poorly stabilized, and the distribution of Ni, Fe, and Mn inside the particles is not homogeneous. The selected time window, therefore, corresponds to the range in which nucleation and compositional homogenization are achieved.

Our findings reveal that these parameters have distinct yet interconnected effects on the properties of the active material. The temperature mainly affects particle aggregation and crystallinity, while reaction time affects primary particle size and the relative amount of the O3 and P2 phases. In particular, increasing the temperature decreases aggregation, while increasing reaction time favors the formation of smaller particles with a higher fraction of the P2 phase. Galvanostatic cycling at progressively higher currents reveals that the sample synthesized at 60 °C for 9 h delivers the best rate capability, reaching a specific capacity of about 130 mAh g^{-1} at 0.1 C and maintaining good reversibility at higher C-rates. However, its higher O3 phase content leads to a pronounced capacity fading during cycling, due to irreversible structural transitions typical of O3-type layered oxides. In contrast, samples with a higher P2 phase content (longer synthesis) exhibit better structural stability and, therefore, higher capacity retention during cycling. However, this comes at the expense of specific capacity.

Overall, this work highlights the delicate interplay between synthesis parameters and the phase composition, morphology, and electrochemical behavior of the resulting material. Therefore, these insights provide valuable guidance for future materials design, demonstrating that careful optimization of both temperature and time is essential to achieve materials with superior structural quality and electrochemical

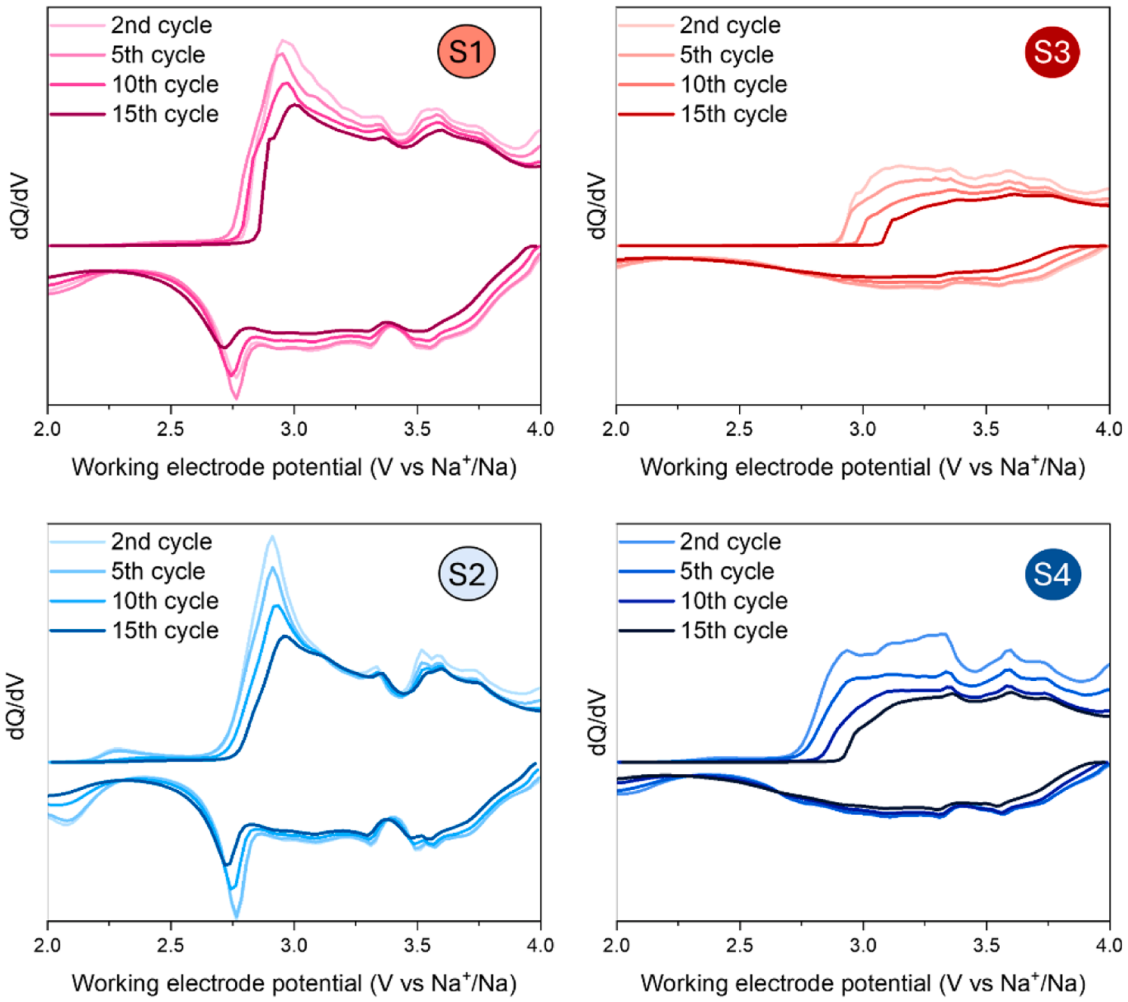

Fig. 5. Differential capacity analysis for S1-S4 obtained by differentiating the Q vs V profile during a galvanostatic cycle at 0.1 C within the 2 – 4 V window vs. Na^+/Na, for the 2nd, 5th, 10th, and 15th cycles.

functionality. In future work, additional synthesis parameters such as reagent concentration, stirring rate, and pH control will be systematically investigated to further elucidate their influence on precursor formation and the resulting electrochemical behavior of the final oxide.

CRediT authorship contribution statement

Valeria Sperati: Writing – original draft, Visualization, Methodology, Formal analysis. **Hamideh Darjazi:** Writing – review & editing, Visualization, Methodology, Investigation. **Alessandro Piovano:** Writing – review & editing, Visualization, Methodology, Investigation. **Marco Ricci:** Writing – review & editing, Validation, Methodology, Investigation. **Claudio Gerbaldi:** Writing – review & editing, Validation, Supervision, Funding acquisition, Formal analysis. **Giuseppe Antonio Elia:** Writing – review & editing, Visualization, Supervision, Funding acquisition, Formal analysis. **Remo Proietti Zaccaria:** Writing – review & editing, Validation, Supervision, Funding acquisition, Formal analysis.

Declaration of competing interest

The authors declare that they have no known competing financial interests or personal relationships that could have appeared to influence the work reported in this paper.

Acknowledgment

This study was carried out within the GENESIS project –funded by the Ministero dell'Università e della Ricerca – within the PRIN 2022 program (D.D.104 - 02/02/2022). This research was supported by Italian Ministry of Economic Development through ENEA in the frame of the "Ricerca Sistema Elettrico" PTR program 2025–2027. Authors acknowledge support by the National Recovery and Resilience Plan (PNRR), within the NEST – Network 4 Energy Sustainable Transition (Mission 4, Component 2, Investment 1.3 – D.D. 1561 11.10.2022 of the Ministero dell'Università e della Ricerca (MUR), PE0000021), which received funding from the European Union Next-GenerationEU (PNRR eMission 4, Component 2, Investment 1.4 and D.D. 1033 17/06/2022 of the MUR, CN00000023). This manuscript reflects only the authors' views and opinions, neither the European Union nor the European Commission can be considered responsible for them. Support under the MUR program "Dipartimenti di Eccellenza 2023–2027" (CUPE17G22001490006) is gratefully acknowledged.

Supplementary materials

Supplementary material associated with this article can be found, in the online version, at doi:10.1016/j.electacta.2026.149276.

Data availability

Data will be made available on request.

References

[1] F. Wang, Y. You, Y.-X. Yin, Y.-G. Guo, Layered oxide cathodes for sodium-ion batteries: phase transition, air stability, and performance, Adv. Energy Mater. 8 (2018) 1701912, https://doi.org/10.1002/aenm.201701912.

[2] M.H. Han, E. Gonzalo, G. Singh, T. Rojo, A comprehensive review of sodium layered oxides: powerful cathodes for Na-ion batteries, Energy Environ. Sci. 8 (2015) 81–102, https://doi.org/10.1039/c4ee03192j.

[3] C. Delmas, C. Fouassier, P. Hagenmuller, Structural classification and properties of the layered oxides, Physica B+C 99 (1980) 81–85, https://doi.org/10.1016/0378-4363(80)90214-4.

[4] I. Hasa, J. Barker, G. Elia, S. Passerini, Battery types – sodium batteries – low-temperature sodium batteries. Overview. Encyclopedia of Electrochemical Power Sources 2nd ed., 4, Elsevier, 2025, pp. 767–784, https://doi.org/10.1016/B978-0-323-96022-9.00061-X.

[5] Y. Sun, P. Zhou, S. Liu, Z. Zhao, Y. Pan, X. Shen, X. Wu, J. Zhao, J. Weng, J. Zhou, Manipulating Na occupation and constructing protective film of P2-Na0.67Ni0.33Mn0.67O2 as long-term cycle stability cathode for sodium-ion batteries, J. Energy Chem. 88 (2024) 603–611, https://doi.org/10.1016/j.jechem.2023.09.042.

[6] A. Massaro, A.B. Muñoz-García, P.P. Prosini, C. Gerbaldi, M. Pavone, Unveiling oxygen redox activity in P2-type NaxNi0.25Mn0.68O2 high-energy cathode for Na-ion batteries, ACS Energy Lett. 6 (2021) 2470–2480, https://doi.org/10.1021/acsenergylett.1c01020.

[7] C. Lee, M. Shimizu, R. Tatara, K. Nakamoto, T. Hosaka, Z.T. Gossage, S. Komaba, Synergistic effects of Na2CO3 as sacrificial salt and water-soluble binder for Na-ion battery with Na-deficient P2-Na2/3Ni1/3Mn2/3O2, ACS Appl. Energy Mater. 8 (2025) 5867–5877, https://doi.org/10.1021/acsaem.5c00289.

[8] S. Lin, H. Zhang, C. Shu, W. Hua, X. Wang, Y. Zhao, J. Luo, Z. Tang, Y. Wu, W. Tang, Research progress and perspectives on pre-sodiation strategies for sodium-ion batteries, Adv. Funct. Mater. 34 (2024) 2409628, https://doi.org/10.1002/adfm.202409628.

[9] M. Sathiya, J. Thomas, D. Batuk, V. Pimenta, R. Gopalan, J.M. Tarascon, Dual stabilization and sacrificial effect of Na2CO3 for increasing capacities of Na-ion cells based on P2-NaxMO2 electrodes, Chem. Mater. 29 (2017) 5948–5956, https://doi.org/10.1021/acs.chemmater.7b01542.

[10] F. Ding, C. Zhao, D. Zhou, Q. Meng, D. Xiao, Q. Zhang, Y. Niu, Y. Li, X. Rong, Y. Lu, L. Chen, Y.S. Hu, A novel Ni-rich O3-Na[Ni0.60Fe0.25Mn0.15]O2 cathode for Na-ion batteries, Energy Storage Mater. 30 (2020) 420–430, https://doi.org/10.1016/j.ensm.2020.05.013.

[11] X. Gao, L. Fang, H.J. Wang, S. Lee, H. Liu, S. Zhang, J. Gao, Y. Mei, M. Park, J. Zhang, M. Chen, L. Zhou, W. Deng, G. Zou, H. Hou, Y.M. Kang, X. Ji, Origin of fast capacity decay in Fe–Mn based sodium layered oxides, Adv. Funct. Mater. 33 (2023) 2212685, https://doi.org/10.1002/adfm.202212685.

[12] C. Jiang, Y. Wang, Y. Xin, X. Ding, S. Liu, Y. Pang, B. Chen, Y. Wang, L. Liu, F. Wu, H. Gao, Toward high stability of O3-type NaNi1/3Fe1/3Mn1/3O2 cathode material with zirconium substitution for advanced sodium-ion batteries, Carbon Neutraliz. 3 (2024) 233–244, https://doi.org/10.1002/cnl2.115.

[13] H. Jung, J. Kim, S. Kim, Phonon study of Jahn–Teller distortion and phase stability in NaMnO2 for sodium-ion batteries, J. Appl. Phys. 132 (2022) 085101, https://doi.org/10.1063/5.0086903.

[14] M. Palluzzi, L. Silvestri, A. Celeste, M. Tuccillo, A. Latini, S. Brutti, Structural degradation of O3-NaMnO2 positive electrodes in sodium-ion batteries, Crystals 12 (2022) 885, https://doi.org/10.3390/cryst12070885.

[15] J.Y. Hwang, S.T. Myung, D. Aurbach, Y.K. Sun, Effect of nickel and iron on structural and electrochemical properties of O3 type layer cathode materials for sodium-ion batteries, J. Power Sources 324 (2016) 106–112, https://doi.org/10.1016/j.jpowsour.2016.05.064.

[16] W. Wang, Y. Sun, P. Wen, Y. Zhou, D. Zhang, Enhanced conduction and phase transition reversibility of O3-type NaNi1/3Fe1/3Mn1/3O2 cathode via Ta doping for high-performance sodium-ion battery, J. Energy Storage 79 (2024) 110177, https://doi.org/10.1016/j.est.2023.110177.

[17] K. Fang, J. Yin, G. Zeng, Z. Wu, Y. Tang, D. Yu, H. Luo, Q. Liu, Q. Zhang, T. Qiu, H. Huang, Z. Ning, C. Ouyang, L. Gu, Y. Qiao, S.G. Sun, Elucidating the structural evolution of O3-type NaNi1/3Fe1/3Mn1/3O2: a prototype cathode for Na-ion battery, J. Am. Chem. Soc. 146 (2024) 31860–31872, https://doi.org/10.1021/jacs.4c11049.

[18] W. Chen, Y. Chi, Y. Wang, W. Yang, H. Zou, S. Chen, Controllable synthesis of P2/O3 NaxNi0.33Mn0.33Fe0.33O2 single-crystal oxides through a sodium alginate sol-gel method for advanced sodium-ion batteries, J. Power Sources 636 (2025) 236570, https://doi.org/10.1016/j.jpowsour.2025.236570.

[19] Y. Chang, Y. Zhou, Z. Wang, X. Li, D. Wang, J. Duan, J. Wang, G. Yan, Synthesis of NaNi0.5Mn0.5O2 cathode materials for sodium-ion batteries via spray pyrolysis method, J. Alloys Compd. 922 (2022) 166283, https://doi.org/10.1016/j.jallcom.2022.166283.

[20] R.A.H. Gayara, B. Moossa, R.A. Shakoor, R.F. Shahzad, M. Sajjad, N. Singh, S. Rasul, T.M. Al Tahtamouni, Cost-effective microwave-assisted O3-type sodium-based layered oxide cathode materials for sodium-ion batteries, Energy Rep. 10 (2023) 837–849, https://doi.org/10.1016/j.egyr.2023.07.038.

[21] J. Li, H. Hu, J. Wang, Y. Xiao, Surface chemistry engineering of layered oxide cathodes for sodium-ion batteries, Carbon Neutraliz. 1 (2022) 96–116, https://doi.org/10.1002/cnl2.19.

[22] Y.J. Guo, R.X. Jin, M. Fan, W.P. Wang, S. Xin, L.J. Wan, Y.G. Guo, Sodium layered oxide cathodes: properties, practicality and prospects, Chem. Soc. Rev. 53 (2024) 7828–7874, https://doi.org/10.1039/d4cs00415a.

[23] Z. Zhang, Y. Liu, Z. Liu, H. Li, Y. Huang, W. Liu, D. Ruan, X. Cai, X. Yu, Dual-strategy of Cu-doping and O3 biphasic structure enables Fe/Mn-based layered oxide for high-performance sodium-ion batteries cathode, J. Power Sources 567 (2023) 232930, https://doi.org/10.1016/j.jpowsour.2023.232930.

[24] H. Cui, C. Yang, H. Zhou, X. Cai, J. Chang, Synergistic enhancement of O3-NaNi0.33Fe0.33Mn0.33O2 cathodes via La doping and solvent-free high-energy ball-milling for advanced sodium-ion batteries, J. Energy Storage 133 (2025) 118068, https://doi.org/10.1016/j.est.2025.118068.

[25] S.Y. Lee, J.H. Kim, Y.C. Kang, Electrochemical properties of P2-type Na2/3Ni1/3Mn2/3O2 plates synthesized by spray pyrolysis process for sodium-ion batteries, Electrochim. Acta 225 (2017) 86–92, https://doi.org/10.1016/j.electacta.2016.11.141.

[26] J. Jamboretz, Y. Zhu, R. James, L. Mu, C.S. Birkel, Microwave-assisted synthesis of P2- and O3-type NaxCoO2 cathode materials studied by in situ Raman spectroscopy, Chem. Mater. 36 (2024) 8447–8457, https://doi.org/10.1021/acs.chemmater.4c01551.

[27] G.-T. Park, H.-H. Ryu, N.-Y. Park, S.-B. Lee, Y.-K. Sun, Single-crystal vs polycrystalline cathodes for lithium-ion batteries, Chem. Rev. 125 (2025) 9930–10000, https://doi.org/10.1021/acs.chemrev.5c00441.

[28] P. Saengkwamsawang, P. Katekaew, A. Klinbumrung, Dissolution recrystallization growth and structural characteristics of facile decomposition-processed NiFe2O4 octahedrons, J. Cryst. Growth 633 (2024) 127648, https://doi.org/10.1016/j.jcrysgro.2024.127648.

[29] Y. Jiang, F. Zhou, C. Wang, J. Kong, L. Xu, Influence of co-precipitation temperature on microstructure and electrochemical properties of Li[Li0.2Mn0.54Ni0.13Co0.13]O2 cathode materials for lithium ion batteries, Ionics 23 (2017) 585–596, https://doi.org/10.1007/s11581-016-1863-2.

[30] D. Ren, Y. Shen, Y. Yang, L. Shen, B.D.A. Levin, Y. Yu, D.A. Muller, H.D. Abruña, Systematic optimization of battery materials: key parameter optimization for the scalable synthesis of uniform, high-energy, and high stability LiNi0.6Mn0.2Co0.2O2 cathode material for lithium-ion batteries, ACS Appl. Mater. Interfaces 9 (2017) 35811–35819, https://doi.org/10.1021/acsami.7b10155.

[31] Y. Shen, Y. Wu, H. Xue, S. Wang, D. Yin, L. Wang, Y. Cheng, Insight into the coprecipitation-controlled crystallization reaction for preparing lithium-layered oxide cathodes, ACS Appl. Mater. Interfaces 13 (2021) 717–726, https://doi.org/10.1021/acsami.0c19493.

[32] H. Zhao, J. Li, W. Liu, H. Xu, X. Gao, J. Shi, K. Yu, X. Ding, Integrated titanium-substituted air stable O3 sodium layered oxide electrode via a complexant assisted route for high capacity sodium-ion battery, Electrochim. Acta 388 (2021) 138561, https://doi.org/10.1016/j.electacta.2021.138561.

[33] V. Diolaiti, A. Andreoli, S. Fugattini, M. Ricci, S. Mondal, D. Giubertoni, E. Venezia, M. Prato, S. Marras, S. Dante, A. Pegoretti, R. Dell'Anna, R.P. Zaccaria, D. Vincenzi, Operando structural rearrangement of self-ion-implanted germanium films enables high-rate cycling in lithium-ion batteries, Phys. Status Solidi 223 (2026) e202500878, https://doi.org/10.1002/pssa.202500878.

[34] Q. Wang, C. Zhao, M. Wagemaker, Rational design of layered oxide materials for batteries, Acc. Chem. Res. 58 (2025) 1742–1753, https://doi.org/10.1021/acs.accounts.5c00074.

[35] C. Zhao, Q. Wang, Z. Yao, J. Wang, B. Sánchez-Lengeling, F. Ding, X. Qi, Y. Lu, X. Bai, B. Li, H. Li, A. Aspuru-Guzik, X. Huang, C. Delmas, M. Wagemaker, L. Chen, Y.S. Hu, Rational design of layered oxide materials for sodium-ion batteries, Science 370 (2020) 708–711, https://doi.org/10.1126/science.aay9972.

[36] J.N. Israelachvili. Intermolecular and Surface Forces, 3rd ed., Academic Press - Elsevier, New York, USA, 2011, ISBN 9780123919274.

[37] M. Bianchini, J. Wang, R.J. Clément, B. Ouyang, P. Xiao, D. Kitchaev, T. Shi, Y. Zhang, Y. Wang, H. Kim, M. Zhang, J. Bai, F. Wang, W. Sun, G. Ceder, The interplay between thermodynamics and kinetics in the solid-state synthesis of layered oxides, Nat. Mater. 19 (2020) 1088–1095, https://doi.org/10.1038/s41563-020-0688-6.

[38] S. Zhao, Q. Shi, W. Feng, Y. Liu, X. Yang, X. Zou, X. Lu, Y. Zhao, Research progresses in O3-type Ni/Fe/Mn based layered cathode materials for sodium ion batteries, Carbon Neutrality 2 (2023) 53, https://doi.org/10.1007/s43979-023-00053-9.

[39] A. Ghosh, R. Hegde, P. Senguttuvan, A high entropy O3-Na1.0Li0.1Ni0.3Fe0.1Mn0.25Ti0.25O2 cathode with reversible phase transitions and superior electrochemical performances for sodium-ion batteries, J. Mater. Chem. A 12 (2024) 14583–14594, https://doi.org/10.1039/d4ta01137f.

[40] G. Pang, Y. Gu, H. Zhuo, M. Li, K. Wang, J. Wang, D. Wang, J. Hu, B. Xiao, W. Zhuang, A holistic picture of the phase construction process of O3-structured NaNi1/3Mn1/3Fe1/3O2 for sodium-ion batteries, Adv. Funct. Mater. 35 (2025) 2505824, https://doi.org/10.1002/adfm.202505824.

[41] B. Xiao, X. Liu, M. Song, X. Yang, F. Omenya, S. Feng, V. Sprenkle, K. Amine, G. Xu, X. Li, D. Reed, A general strategy for batch development of high-performance and cost-effective sodium layered cathodes, Nano Energy 89 (2021) 106371, https://doi.org/10.1016/j.nanoen.2021.106371.

[42] H. Yang, Q. Zhang, M. Chen, Y. Yang, J. Zhao, Unveiling the origin of air stability in polyanion and layered-oxide cathode materials for sodium-ion batteries and their practical application considerations, Adv. Funct. Mater. 34 (2024) 2308257, https://doi.org/10.1002/adfm.202308257.

[43] K. Wang, H. Zhuo, J. Wang, F. Poon, X. Sun, B. Xiao, Recent advances in Mn-rich layered materials for sodium-ion batteries, Adv. Funct. Mater. 33 (2023) 2212607, https://doi.org/10.1002/adfm.202212607.
[44] Y. Yang, Z. Wang, C. Du, B. Wang, X. Li, S. Wu, X. Li, X. Zhang, X. Wang, Y. Niu, F. Ding, X. Rong, Y. Lu, N. Zhang, J. Xu, R. Xiao, Q. Zhang, X. Wang, W. Yin, J. Zhao, L. Chen, J. Huang, Y.-S. Hu, Decoupling the air sensitivity of Na-layered oxides, Science 385 (2024) 744–752, https://doi.org/10.1126/science.adm9223.
[45] H.R. Yao, L. Zheng, S. Xin, Y.G. Guo, Air-stability of sodium-based layered-oxide cathode materials, Sci. China Chem. 65 (2022) 1076–1087, https://doi.org/10.1007/s11426-022-1257-8.
[46] A. Langella, A. Massaro, A.B. Muñoz-García, M. Pavone, Atomistic insights into solid-state phase transition mechanisms of P2-type layered Mn oxides for high-energy Na-ion battery cathodes, ACS Energy Lett. 10 (2025) 1089–1098, https://doi.org/10.1021/acsenergylett.4c03335.
[47] H. Li, L. Wang, Y. Song, Z. Zhang, A. Du, Y. Tang, J. Wang, X. He, Why the synthesis affects performance of layered transition metal oxide cathode materials for li-ion batteries, Adv. Mater. 36 (2024) 2312292, https://doi.org/10.1002/adma.202312292.
[48] Q. Lu, T. Shen, Y. Zeng, Y. Zhou, M. Su, Z. Sun, L. Liu, A. Jiang, Y. Wan, Y. Liu, R. Wang, Medium-entropy doping in Na4Fe3(PO4)2P2O7 cathode via Mg/Cu/Cr triple doping: site-specific optimization unlocks high conductivity and ultralong cyclability, Adv. Funct. Mater 35 (2025) e09628, https://doi.org/10.1002/adfm.202509628.
[49] X. Zhao, L. Hou, Q. Liu, Y. Zhao, D. Mu, Z. Zhao, L. Li, R. Chen, F. Wu, Insights into the capacity fading and failure mechanism of an O3-NaNi1/3Fe1/3Mn1/3O2 layered oxide cathode material for sodium-ion batteries, J. Mater. Chem. A Mater. 12 (2024) 12443–12451, https://doi.org/10.1039/d4ta00060a.
[50] G. Zhang, Y. Gao, Y. Fan, Y. Gao, J. Wu, J. Ma, R. Zhang, Y. Huang, Boosting the structural reversibility of layered oxide cathode for realizing long-term cycle life through electronic structure regulation, Small 20 (2024) 2407615, https://doi.org/10.1002/smll.202407615.
[51] S. Luan, J. Xie, R. Cai, Insight into LaFeO3-coating effects on O3-Type NaNi1/3Fe1/3Mn1/3O2 cathode materials for sodium-ion battery application, Energy Fuels 39 (2025) 12264–12272, https://doi.org/10.1021/acs.energyfuels.5c01717.